Journal of Solid State Chemistry 183 (2010) 1409–1415

Contents lists available at ScienceDirect

Journal of Solid State Chemistry

journal homepage: www.elsevier.com/locate/jssc

Controllable preparation and fluorescence properties of Y^{3+} and Eu^{3+} co-doped mesoporous silica

Chao Zhang [a], Shanyi Guang [b,**], Hongyao Xu [a,c,*]

[a] College of Material Science and Engineering & State Key Laboratory of Chemical Fibers and Polymeric Materials, Donghua University, Shanghai 201620, China
[b] College of Chemistry and Chemical Engineering & Biology Engineering, Donghua University, Shanghai 201620, China
[c] State Key laboratory of Crystal Material, Shandong University, Jinan 250100, China

ARTICLE INFO

Article history:
Received 20 November 2009
Received in revised form
26 February 2010
Accepted 10 April 2010

Keywords:
RE co-doped
Well ordered
Mesoporous silica
Fluorescence

ABSTRACT

The controllable preparation and forming mechanism of rare-earth Y^{3+} and Eu^{3+} chemically co-doped fluorescent mesoporous silica were studied in detail. Their structures, morphologies, chemical compositions and emission properties were characterized and evaluated by small angle X-ray scattering, nitrogen adsorption/desorption measurements, high resolution transmission electron microscopy, inductive coupled plasma-atomic emission, X-ray photoelectron spectra and fluorescent spectroscopy. The results show that chemical composition of the resultant mesoporous materials were significantly affected by solution acidity condition, and can be effectively adjusted by varying the feed ratio of raw materials at a suitable solution acidity condition. These materials with a well-ordered two-dimensional hexagonal mesoporous structure and high specific surface area exhibit significantly broadened emission band from 526 to 682 nm and the fluorescent emission mechanism and influence of materials structure on optical properties were investigated.

1. Introduction

The generation of structure-controllable and detectable drug delivery system has drawn considerable attention owing to the vital significance in the human health care and biomedical materials science [1–4]. Mesoporous silica such as M41S and SBA-15 have been demonstrated strong ability in controlled-release systems due to their features of the ordered pore network, high pore volume and surface area with rich silanol group [5–15]. The advancement of smart drug delivery materials, from one spot, requires the in-situ detection and trace technique in the biological system [16–19]. As well known, fluorescent labeling is an effective method applied in biomedical detection. Rare-earth (RE) ions doped materials are ideal candidates for the fluorescent detection due to their high luminescence stability and non-toxicity compared with organic or hybrid phosphors [20–23]. Therefore, a great deal of effort has been devoted to prepare RE blended mesoporous materials [24,25]. Nevertheless, so far these mesoporous materials are generally doped with RE oxides or salts nanoparticles by post-synthesis method (This method is putting synthesized mesoporous materials into the solution or sol containing RE ions to form RE oxides or salts nanoparticles in porous channel.), this simple post-synthesis method often leads to the jam or blockage of the partial porous channel and the uneven distribution of nanometer RE oxides or salts in the mesoporous materials, which results in destruction of the pore structures and decreases the drug loading efficiency. The direct incorporation or chemical doping of RE ions into mesoporous materials will effectively overcome the defect. In the paper, the hydrolytic condensation coprecipitation synthesis approach was employed to directly prepare novel well-ordered Y^{3+} and Eu^{3+} directly co-doped mesoporous silica (RE-SBA-15). The controllable preparation, formation mechanism and relationship between their structures and fluorescence properties were investigated.

2. Experimental

2.1. Chemicals

Tetraethyl orthosilicate (TEOS), yttrium oxide (Y_2O_3), europium oxide (Eu_2O_3) and hydrochloric acid (HCl) were used as the sources for silica, ion (III) and catalyst, all of which were purchased from Shanghai Chemicals Ltd. Yttrium nitrate ($Y(NO_3)_3$) and europium nitrate ($Eu(NO_3)_3$) were prepared by the reaction of Y_2O_3 and Eu_2O_3 with nitric acid (HNO_3) purchased from Shanghai Chemicals Ltd. Triblock copolymer poly(ethylene

* Corresponding author at: State Key Laboratory of Chemical Fibers and Polymeric Materials, College of Material Science and Engineering, Donghua University, North Renmin Road, Shanghai 201620, China. Fax: +86 21 67792874.
** Also Corresponding author.
E-mail addresses: syg@dhu.edu.cn (S. Guang), hongyaoxu@163.com (H. Xu).

0022-4596/$ - see front matter © 2010 Elsevier Inc. All rights reserved.
doi:10.1016/j.jssc.2010.04.013

glycol)-*block*-poly-(propylene glycol)-*block*-poly(ethylene glycol) (Pluronic P123, molecular weight 5800, $EO_{20}PO_{70}EO_{20}$) as the structure-directing template was purchased from Aldrich.

2.2. Synthesis

A series of Y^{3+} and Eu^{3+} co-doped mesoporous silica (RE-SBA-15) with various n_{Si}/n_{RE} (fixed n_Y/n_{Eu} ratios) and n_Y/n_{Eu} ratios (fixed n_{Si}/n_{RE} ratios) were prepared by hydrolytic condensation coprecipitation/hydrothermal synthesis approach [26–30]. In a typical synthesis of RE-SBA-15, 2.0 g of Pluronic P123 was dissolved in 30 mL water to get a clear solution. Thereafter, the required amount of dilute HCl solution was added, and the solution was again stirred for another 1 h to mix with the hydronium ions of the alkylene oxide units. Then, 4.2 g of TEOS and the required amount of $Y(NO_3)_3$ and $Eu(NO_3)_3$ solution were added, and the resulting mixture was stirred for 24 h at 35 °C and then reacted hydrothermally at 90 °C for another 48 h in static condition. The product was filtered, washed with deionised water, and dried at 70 °C. Finally, the as-synthesized RE-SBA-15 samples were heated at 250 °C for 2 h and then at 500 °C for another 4 h to obtain the calcined porous samples by removing Pluronic P123.

2.3. Design of samples

The first set of samples were prepared at a fixed n_{Si}/n_{RE} ratio of 5 and n_Y/n_{Eu} ratio of 4 by changing the acidity of the solution (HCl concentration: c=0.15, 0.30, 0.45 and 0.60 mol/L). The second set of RE-SBA-15 samples were prepared at a fixed n_Y/n_{Eu} molar ratio of 4 and substance concentration of HCl of 0.45 mol/L by varying the n_{Si}/n_{RE} ratios (n_{Si}/n_{RE}=2.0, 5.0, 10, 20 and 40). The third set of samples were obtained at a fixed n_{Si}/n_{RE} ratio of 5 and concentration of HCl of 0.45 mol/L (0.45 mol/L HCl) by changing the n_Y/n_{Eu} ratios (n_Y/n_{Eu}=9.0, 5.7, 4.0, 3.0 and 2.3).

2.4. Preparation of RE-doped nanoparticles (RE-NPs)

For comparison, the Y^{3+} and Eu^{3+} co-doped nanoparticle SiO_2 were prepared by sol–gel method, which consisted of the n_{Si}/n_{RE} ratio of 5.15 and n_Y/n_{Eu} ratios of 3.94. In the specific procedure, 1.72 g $Y(NO_3)_3$ and 0.53 g $Eu(NO_3)_3$ were dissolved in 25 mL of water to get a clear solution, thereafter, 8.4 g TEOS and 5 mL HCl solution (3 mol/L) were added, and the resulting mixture was stirred for 2 h at 60 °C and then transferred into closed vessel in static condition to form gel. The gel was heated at 500 °C for 4 h to obtain the calcined samples.

2.5. Characterization

XRD patterns were recorded by a Philip X'pert Pro diffractometer with Cu $K\alpha$ radiation and operated at 40 mA and 45 kV in the 2θ range 10–60°. The nitrogen adsorption–desorption measurements of the mesoporous materials were performed on a Micromeritics ASAP 2020M+C Surface Area and Porosimetry Analyzer, in which the samples were outgased at 300 °C for 8 h under vacuum (10^{-3} Torr) in the degas port of the adsorption analyzer. The surface area was calculated by the Brunauer–Emmett–Teller (BET) method, and pore size distribution was derived from the adsorption branches of the isotherms using the Barrett–Joyner–Halenda (BJH) method. Element component contents in resulting materials were determined by a Leeman Prodigy ICP-AES (Thermo Electro, IRIS Intrepid II) after the samples were dissolved in a HF solution. Small-angle X-ray scattering (SAXS) patterns were recorded on a Bruker Nanostar U diffractometer using Cu $K\alpha$ radiation (1.54 Å) with a distance 107 cm of sample to detector, in which the X-ray tube was operated at 40 kV and 30 mA while the diffractograms were recorded in the 2θ range 0.4–2.8° with a 2θ step size of 0.01 and a step time of 10 s. Transmission electron microscopy (TEM) images were recorded using a JEOL 2010 instrument operated at 200 kV. For TEM imaging, samples were dispersed in ethanol and deposited on carbon-coated copper grids. High resolution solid state ^{29}Si NMR (nuclear magnetic resonance) spectra were obtained on a Bruker AC 300 NMR spectrometer operating at resonance frequency of 79.38 MHz. X-ray photoelectron spectroscopy (XPS) measurements were performed on an ECSALAB 250 using a nonmonochromatized Al $K\alpha$ radiation, at a working pressure lower than 10^{-9} mbar. Excitation and emission spectra at room (298 K) temperature were collected at an angle of 22.5 (front face) in a spectrofluorimeter (Jasco FP6600) with a 150 W xenon lamp as excitation source; and excitation/emission slits are 5 and 6 nm, respectively; otherwise the same mass of all the RE-SBA-15 samples were put in the solid sample cell for test. Particle size distribution was measured on a Mastersizer 2000 laser particle size analyzer.

3. Results and discussion

3.1. The controllable preparation and forming mechanism

The chemical component contents of these resultant RE-SBA-15 samples were determined by ICP method and the results were summarized in Table 1. It can be seen from Table 1 that at relative low and high solution acidity the component contents in resulting products significantly deviate from the feed ratio (n_{Si}/n_{RE}). For example, the n_{Si}/n_{RE} ratio changes from original feed ratio 5:1 to practical 11.82:1 in the resulting materials obtained in a solution acidity of 0.15 M HCl (Table 1, no. 1), and 5:1 to 46.72:1 in a solution acidity of 0.60 M HCl (Table 1, no. 4). However, the component contents (n_{Si}/n_{RE} ratio) of the resultant products are close to the feed ratios at 0.45 M HCl concentration (Table 1, no. 3), suggesting that the acidity of reaction system significantly affects the component contents in resultant materials and a suitable solution acidity in the reaction system (0.45 M HCl) will play a key role to actualize the effective control of chemical component contents of these mesoporous silica.

To investigate the deviation reason of component contents at relatively low or high solution acidity and the influence mechanism of solution acidity, we used the aqueous ammonia to neutralize the clear filtrate of each sample to pH values 10.0. The white flocculent precipitates were observed in the clear filtrate with HCl concentration of 0.30, 0.15, or 0.60 M (Table 1, no. 1, 2, 4), which were confirmed to be RE ions hydroxide. The precipitate amount significantly increases with the increment of deviation value in the resulting materials. However, almost no significant precipitate was observed in the filtrate with HCl concentration of 0.45 M, hinting that the rare-earth elements were almost completely incorporated into the resultant mesoporous materials. The solid precipitate in other three samples were

Table 1
Elemental analysis on RE-SBA-15 samples at different concentration of HCl.

Samples	c_{HCl} (mol/L)	Feed ratio		ICP-AES	
		n_Y/n_{Eu}	n_{Si}/n_{RE}	n_Y/n_{Eu}	n_{Si}/n_{RE}
1	0.15	4.0	5.0	3.92	11.82
2	0.30	4.0	5.0	3.94	7.69
3	0.45	4.0	5.0	3.94	5.15
4	0.60	4.0	5.0	3.96	46.72

collected by centrifuging the precipitated solution for 5 min at 6000 r/min, then calcined at 1000 °C for 4 h and weighted to be 33.9%, 56.8% and 88.3% of the mass of the added raw rare-earth ions oxide. They are almost consistent with the amount that is not incorporated into the resultant product; further confirming that the acidity of reaction system significantly affects the component contents in the products. This kind of deviation effect may come from the different hydrolysis rate between the RE ions and TEOS in corresponding acidity solutions. Only when hydrolysis rate of the RE ions matches with that of TEOS, the chemical component can be effectively controlled by varying the feed ratio of raw materials, such as 0.45 M HCl concentration in the system, suggesting that adjusting acidity of the medium is available for quantitative RE ions incorporation into the silica pore walls. The similar phenomenon was also observed in metal-doped SBA-15 [26,29].

In addition, it is also found that the n_Y/n_{Eu} ratio in resulting products is rarely affected by the acidity of the synthetic system, which may be owing to the similar ion radius of Y^{3+} and Eu^{3+}, and almost equal hydrolysis rate under the same condition. On the basis of the above studies, we fixed the overall HCl concentration of 0.45 M in the solution and added different feed ratios of n_{Si}/n_{RE} or n_Y/n_{Eu} in the preparations. It can be seen from Table 2 that the component contents are almost completely consistent with the feed ratio although the feed ratio of n_{Si}/n_{RE} varys from 2.0 to 40.0 (Table 2, no. 1–5) or feed ratio of n_Y/n_{Eu} from 9.0 to 2.3 (Table 2, no. 6–9), further supporting that the component contents in the RE-doped mesoporous silica can be precisely adjusted by varying the feed ratio of raw materials at a suitable solution acidity in current system.

3.2. Structure analysis

The porous structure reflected by 2D SAXS patterns (Fig. 1) manifests that all RE-SBA-15 samples exhibit three well-resolved diffraction peaks indexed as the (100), (110) and (200) reflections in the XRD diffraction pattern, which are contributed to *P6mm* hexagonal space group and are in good agreements with the XRD pattern of pure hexagonally ordered SBA-15 material reported by Zhao et al. [31] indicating that the RE-doped mesoporous silica possess a well-ordered two-dimensional hexagonal porous structure. With the increase of n_{Si}/n_{RE} ratios (n_{Si}/n_{RE}=2.05, 5.15, 10.39, 20.53 and 40.66) (Fig. 1(A)) (Table 2, no. 1–5), the diffraction peak (110) and (200) in the XRD profiles become sharper stage by stage, suggesting that orderliness reduces with the increase of doped RE ions content. However, a clear (100) diffraction peak still remains even at the highest RE content (n_{Si}/n_{RE}=2.05).

Based on Bragg equation, the strongest (100) diffraction peak significantly shifts in the *d*-spacing range from 7.92 to 8.67 nm, which corresponds the unit cell parameters (a) varying from 9.15 to 10.01 nm as calculated from the formula $a=2d_{100}/\sqrt{3}$ (Table 2, no. 1–5). Additionally, it is noted that the wall thicknesses ($W_t=a-d_p$) of the RE-SBA-15 samples increase from 3.56 to 4.43 nm (Table 2, no. 1–5 W_t) with the increasing RE content due to the larger ionic radius of Y^{3+} and Eu^{3+} than Si, and longer bond length of RE–O than Si–O bond. Similar results have also been reported in the metal-substituted mesoporous materials [29,30]. The 2D SAXS patterns of the RE-SBA-15 samples with various n_Y/n_{Eu} ratios (n_Y/n_{Eu}=2.29, 2.98, 3.94, 5.73 and 8.96) (Table 2, no. 6–9) are shown in Fig. 1(B). It can be observed from Fig. 1(B) that three diffraction peaks of all samples with different n_Y/n_{Eu} ratios are indexed to the (100), (110) and (200) diffractions of the

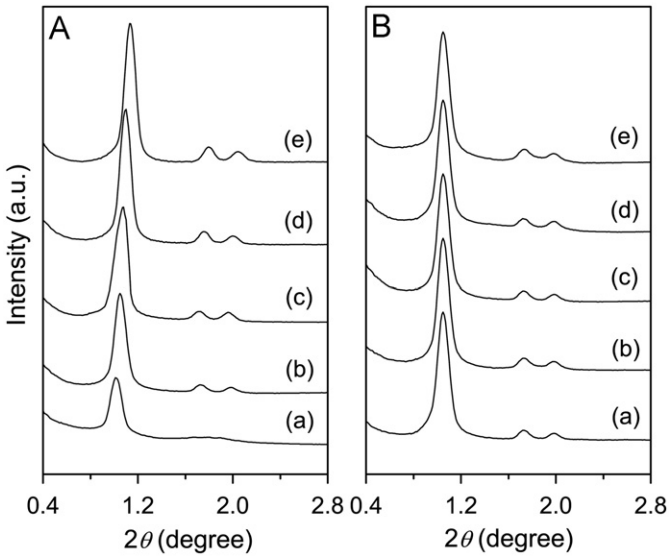

Fig. 1. SAXS patterns of RE-SBA-15 samples (A) at a fixed n_Y/n_{Eu} ratios (ca. 3.95) and different n_{Si}/n_{RE} ratios: (a) 2.05, (b) 5.15, (c) 10.39, (d) 20.53 and (e) 40.66, and (B) at a fixed n_{Si}/n_{RE} ratios (ca. 5.2) and different n_Y/n_{Eu} ratios: (a) 2.29, (b) 2.98, (c) 3.94, (d) 5.73 and (e) 8.96.

Table 2
Textural properties of RE-SBA-15 samples.

Samples	Feed ratio		ICP-AES		a[a] (nm)	A_{BET}[b] (m^2/g)	d_p[c] (nm)	V_p[d] (cm^3/g)	W_t[e] (nm)
	n_Y/n_{Eu}	n_{Si}/n_{RE}	n_Y/n_{Eu}	n_{Si}/n_{RE}					
1	4.0	2.0	3.96	2.05	10.01	805	5.58	0.884	4.43
2	4.0	5.0	3.94	5.15	9.63	905	5.61	1.047	4.02
3	4.0	10.0	3.98	10.39	9.40	934	5.55	1.101	3.85
4	4.0	20.0	3.94	20.53	9.27	1010	5.63	1.213	3.64
5	4.0	40.0	3.95	40.66	9.15	1065	5.59	1.279	3.56
6	9.0	5.0	8.96	5.19	9.64	909	5.59	1.046	4.05
7	5.7	5.0	5.73	5.15	9.59	912	5.60	1.051	3.99
8	3.0	5.0	2.98	5.21	9.58	913	5.61	1.053	3.97
9	2.3	5.0	2.29	5.17	9.60	907	5.58	1.045	4.02
RE-NPs	3.94	5.2	–	–	–	28	–	–	–

[a] The unit cell parameters were calculated from the (100) peaks of the SAXS patterns.
[b] The specific surface areas were obtained from the multiple-point Brunauer–Emmett–Teller (BET) method.
[c] Pore sizes were determined from the N_2 desorption branch by the BJH method with Halsey equation.
[d] The pore volumes were calculated at a relative pressure of 0.97.
[e] Pore wall thicknesses were calculated as a difference between the unit cell parameters, a, and the BJH pore sizes, d_p.

hexagonal space group of *P6mm* and their intensities and peak values are almost the same. The unit cell constants (a) are calculated to be 9.64, 9.59, 9.63, 9.58 and 9.60 nm for the n_Y/n_{Eu} ratios of 2.29, 2.98, 3.94, 5.73 and 8.96 (Table 2, no. 2, 6–9), respectively. In addition, the results show their wall thicknesses (W_t) are approximate at ca. 4.0 nm (Table 2, no. 2, 6–9). The unit cell constant and wall thickness of the RE-SBA-15 samples with different n_Y/n_{Eu} at fixed n_{Si}/n_{RE} (ca. 5.2) are near to each other, suggesting that the n_Y/n_{Eu} ratios hardly affect the unit cell constant and wall thickness of the resulting RE-SBA-15 samples, which are originated from the similar ions radii of doped Y^{3+} and Eu^{3+}.

The specific surface area and pore volume of the RE-SBA-15 samples are shown in Fig. 2A. All isotherms are of type IV according to the IUPAC classification, and exhibit an H1 type hysteresis loop, which is typical of mesoporous solids [31,32]. As the relative pressure increases ($p/p^0 > 0.6$), all isotherms exhibit narrow step characteristic of capillary condensation of nitrogen and the position of the capillary condensation step of relative pressure scarcely shifts with varying n_{Si}/n_{RE} ratios. Additionally, it is also found that the specific surface area and pore volume of the RE-SBA-15 samples are significantly affected by n_{Si}/n_{RE} ratios (n_{Si}/n_{RE}=2.05, 5.15, 10.39, 20.53 and 40.66 are presented in Fig. 2A).

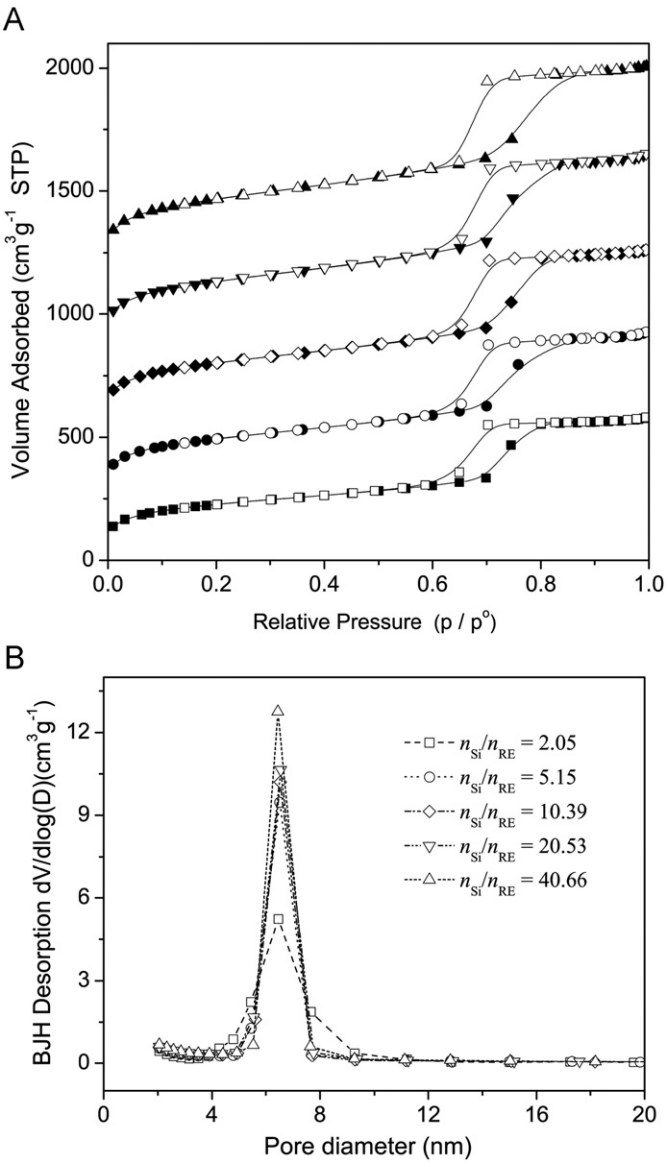

Fig. 2. (A) Nitrogen adsorption isotherm (adsorption: closed symbols; desorption: open symbols) of RE-SBA-15 samples with fixed n_Y/n_{Eu} ratios (ca. 3.95) and different n_{Si}/n_{RE} ratios: (■) 2.05, (●) 5.15, (♦) 10.39, (▲) 20.53 and (▼) 40.66. The isotherms have been offset for clarity (the values of volume adsorbed are 0, 240, 540, 850 and 1170 for n_{Si}/n_{RE} ratios: 2.05, 5.15, 10.39, 20.53 and 40.66, respectively.) (B) BJH Desorption pore size distributions for RE-SBA-15 samples with fixed n_Y/n_{Eu} ratios (ca. 3.95) and different n_{Si}/n_{RE} ratios.

The pore volumes decrease from 1.028 to 0.884 cm^3/g and the specific surface areas decline from 1065 to 805 m^2/g with increasing rare-earth content (Table 2, no. 1–5). However, varying n_Y/n_{Eu} ratios (n_Y/n_{Eu}=2.29, 2.98, 3.94, 5.73 and 8.96) has little effect on the specific surface area and pore volume of the RE-SBA-15 samples (Table 2, no. 2, 6–9).

Fig. 2(B) shows that all the pore sizes for RE-SBA-15 samples obtained from the adsorption branch by the BJH method calculated with Halsey equation are nearly 5.6 nm (Table 2, no. 1–9), indicating the diameters of the RE-SBA-15 samples are hardly influenced by n_Y/n_{Eu} ratios. However, the pore size distribution is apparently broaden at relative high RE ions content (n_{Si}/n_{RE} increasing to 2.05) (Table 2, no. 1), which agrees with the SAXS patterns well. Similar to that of pore volumes and size, various n_Y/n_{Eu} ratios have almost no obvious affection on pore size distribution of the RE-SBA-15 samples.

Fig. 3 shows the transmission electron microscopy (TEM) images of RE-SBA-15 (Table 2, no. 2), which are, respectively, viewed along the direction of the pore axis (Fig. 3(a)) and the direction perpendicular to the pore axis (Fig. 3(b)). The well-ordered hexagonal arrays of mesoporous channels further confirm that RE-SBA-15 has a 2D *p6mm* hexagonal structure. Simultaneously, there are no nanoparticles observed in the porous channels, implying that the Y^{3+} and Eu^{3+} ions are not self-aggregation. Based on the TEM images, the average distance between two consecutive centers of hexagonal pores is estimated to be ca. 9.6 nm and the average thickness of the wall is ca. 4.0 nm, and its pore diameter is around 5.6 nm, which are in agreement with the results obtained from the N_2 adsorption measurements.

The wall structure analysis was carried out by employing solid state ^{29}Si NMR spectra. Fig. 4 shows the solid state ^{29}Si NMR spectrum of RE-SBA-15 (Table 2, no. 2). For comparison, the solid state ^{29}Si NMR spectrum of RE-NPs is also given. The chemical shifts of −90, −101 and −110 ppm are attributed to silica peak of $Si(OSi(RE))_x(OH)_{4-x}$ framework units where x=2 (peak area Q^2 in ^{29}Si NMR spectra), x=3 (Q^3), and x=4 (Q^4), respectively [31]. In general, bulk silica materials mainly exhibit *cross-linked* Q^4 framework unit peak ($[(Q^3+Q^2)/Q^4] < 1$) while RE-NPs samples often possess a high fraction of incompletely cross-linked Q^2 and Q^3 framework unit peaks ($[(Q^3+Q^2)/Q^4] > 1$). Here, the RE-SBA-15 (Table 2, no. 2) exhibits higher fraction of incompletely cross-linked Q^2 and Q^3 framework unit ($[(Q^3+Q^2)/Q^4] \cong 5.26$ than the RE-NPs ($\sim$1.85) with a particle size distribution of 30–50 nm and specific surface area of 28 m^2/g (Table 2), implying that the RE doping mesoporous materials exist more non-bridging oxygen bonds of Si–OH or $Si(OH)_2$, which is in accordance with its high specific surface area of 905 m^2/g.

Fig. 5 displays the XRD patterns of RE-SBA-15 (Table 2, no. 2) and RE-NPs. Both XRD patterns show a diffraction peak with $2\theta = 22^\circ$ being assigning to amorphous SiO_2 without any typical characteristic diffraction peaks of Y_2O_3 (or Eu_2O_3) (JCPDS 29-0085), hinting that the Y^{3+} and Eu^{3+} ions do not produce self-aggregation, but rather uniformly disperse in either wall of mesoporous silica or nanometer silica particles.

Fig. 6 shows the XPS survey spectra of RE-SBA-15 (no. 2) and RE-NPs samples. The XPS spectra revealed the emission peaks correspond to Si, Y, O, C, and Eu in the synthesized samples [33,34]. The calibration of the energy scale was done by using the C1*s* peak at 284.8 eV as a reference. The peaks at about 158.3 and

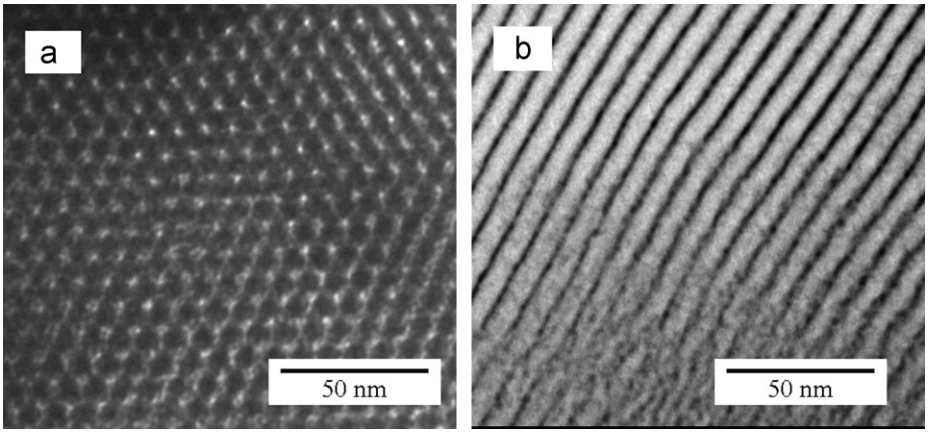

Fig. 3. TEM images of RE-SBA-15 (no. 2) viewed along (a) the direction of the pore axis and (b) the direction perpendicular to the pore axis.

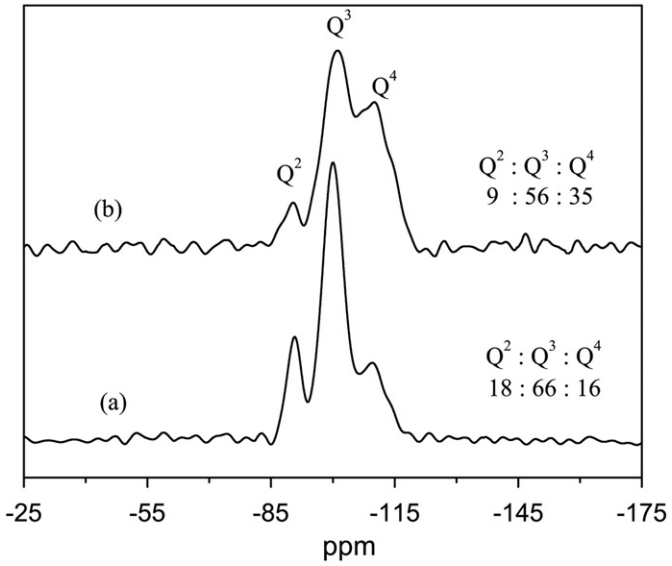

Fig. 4. Solid state ^{29}Si NMR spectra of (a) RE-SBA-15 (no. 2) and (b) RE-NPs both calcined at 500 °C.

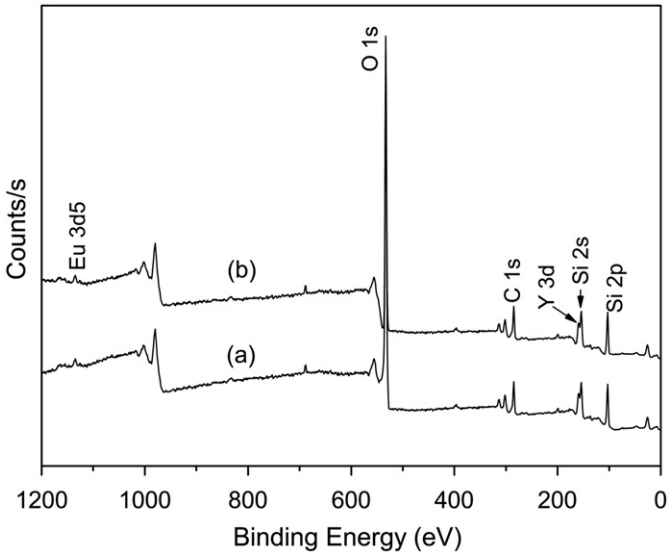

Fig. 6. XPS survey spectra of (a) RE-SBA-15 (no. 2) and (b) RE-NPs both calcined at 500 °C.

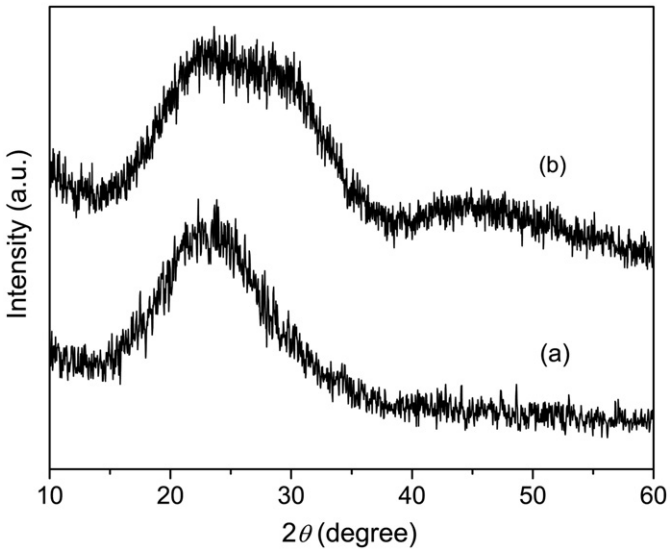

Fig. 5. XRD powder patterns of (a) RE-SBA-15 (no. 2) and (b) RE-NPs both calcined at 500 °C.

Table 3
Surface composition of RE-SBA-15 (no. 2) and RE-NPs estimated through XPS analysis.

Samples	Si (atom %)	O (atom %)	Y (atom %)	Eu (atom %)	n_Y/n_{Eu}	n_{Si}/n_{RE}
2	26.24	68.35	4.36	1.04	4.17	4.86
RE-NPs	27.65	66.74	4.51	1.10	4.10	4.93

1134.6 eV show the binding energies of the $3d_{5/2}$ orbital of Y^{3+} and Eu^{3+} in the corresponding RE-SBA-15 (no. 2) and RE-NPs products. Based on the XPS spectrum, the surface composition of RE-SBA-15 (no. 2) and RE-NPs are estimated and the results are shown in Table 3. It can be seen in Table 3, the n_Y/n_{Eu} and n_{Si}/n_{RE} ratios in the surface of mesoporous wall or nanoparticles is close to that of ICP-AES results, further confirming that Y and Eu homogeneously are distributed into the walls of mesoporous silica or nanometer silica particles.

3.3. Photoluminescence properties

Fig. 7 reveals the excitation and emission spectra of RE-SBA-15 (Table 2, no. 2) and RE-NPs (for comparison). In the excitation

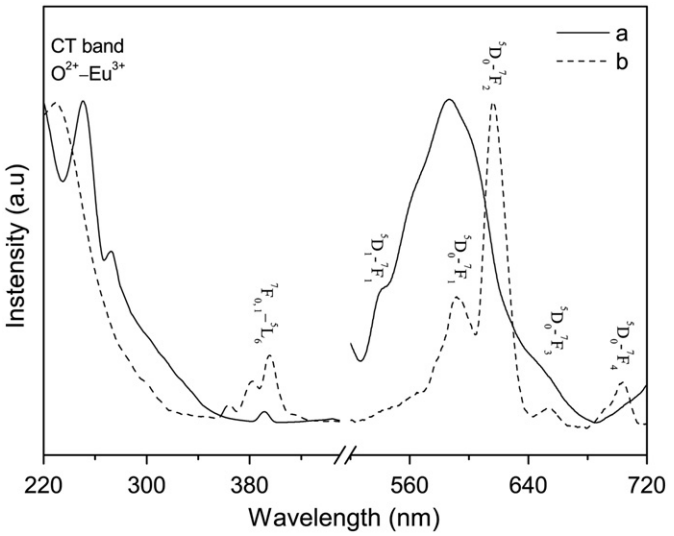

Fig. 7. Room-temperature excitation and emission spectra for (a) RE-SBA-15 (no. 2) (λ_{ex}=250 nm, λ_{em}=588 nm) and (b) RE-NPs (λ_{ex}=231 nm, λ_{em}=616 nm) both calcined at 500 °C. All spectra are normalized to a constant intensity at the maximum.

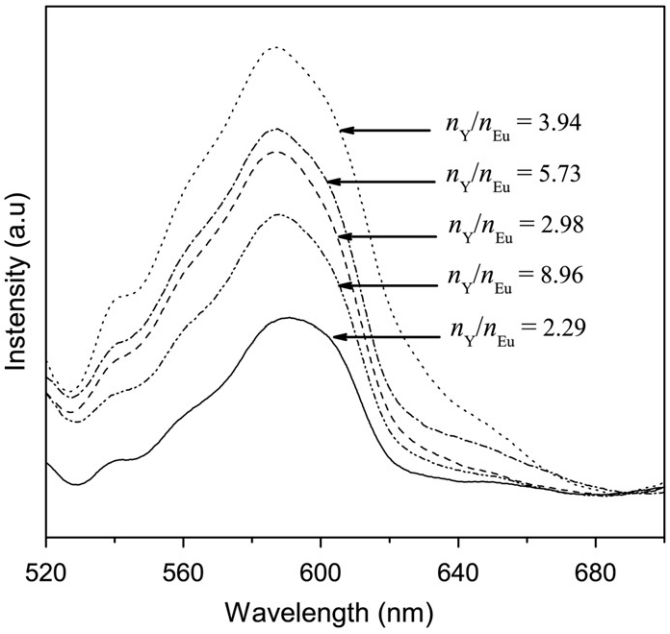

Fig. 8. Room-temperature emission spectra of RE-SBA-15 samples with fixed n_{Si}/n_{RE} ratios (ca. 5.2) and different n_Y/n_{Eu} ratios.

spectra, the charge transfer band (CTB) of RE-NPs is located at 231 nm while CTB of RE-SBA-15 significantly red-shifts to 250 nm. The absorption band at 390 nm arising from the 4*f* to 4*f* transition of inner-shell Eu^{3+} is significantly weakened owing to the decrease of the *cross-linked* Q^4 framework unit. Simultaneously, a new strong absorption shoulder peak at 272 nm is found in the excited spectrum of RE-SBA-15, which is assigned to higher non-bridging oxygen coordinated Eu^{3+} content in the mesopore. This is consistent with that of ^{29}Si NMR spectra. [20,35,36].

In the emission spectra, RE-NPs show the strongest sharp emission peak at 615 nm and four weak emission band at 542, 590, 650 and 700 nm, which are attributed to the transition $^5D_0$–$^7F_2$ (615 nm), $^5D_1$–$^7F_1$ (542 nm), $^5D_0$–$^7F_1$ (590 nm), $^5D_0$–$^7F_3$ (650 nm) and $^5D_0$–$^7F_4$ (700 nm) transitions of Eu^{3+} in the resulting RE-NPs sample, respectively [20,35]. However, RE-SBA-15 shows a significantly broadened emission band in the region from 526 to 682 nm with the main peak located at 588 nm corresponding to the $^5D_0$–$^7F_1$ transitions and four shoulder peaks located at 540, 562, 612 and 654 nm corresponding to $^5D_1$–$^7F_1$, $^5D_0$–$^7F_0$, $^5D_0$–$^7F_2$ and $^5D_0$–$^7F_3$ transitions of Eu^{3+} in the resulting samples, respectively. Such a broad emission profile is originated from the amorphous wall of RE-SBA-15 with high specific surface area. In addition, these large amount of non-bridging oxygen around Eu^{3+} ions also benefit to enhance the relative intensity of magnetic-dipole $^5D_0$–$^7F_1$ of Eu^{3+} in RE-SBA-15 [32,37], which is consistent with the result XRD solid and state ^{29}Si NMR spectra.

The emission spectra of the RE-SBA-15 samples with different n_Y/n_{Eu} ratios excited with 250 nm UV irradiation are shown in Fig. 8. Their emission spectral profiles are identical to each other, indicating that the relative intensity of $^5D_1$–$^7F_1$, $^5D_0$–$^7F_0$, $^5D_0$–$^7F_1$, $^5D_0$–$^7F_2$ and $^5D_0$–$^7F_3$ transitions are hardly affected by different n_Y/n_{Eu}. However, the emission intensity is affected by n_Y/n_{Eu} ratio and the strongest emission band shows at n_Y/n_{Eu} ratio 3.94 with fixed n_{Si}/n_{RE} ratios (ca. 5.2). Similar result was also found in Y^{3+} and Eu^{3+} co-doped nanoparticles in our previous work [23].

4. Conclusions

In conclusion, a series of rare-earth doped mesoporous silica with well-ordered two-dimensional hexagonal structure were controllably prepared. Their chemical component contents can be effectively adjusted by varying raw feed ratio in a suitable acidity condition. These mesoporous materials possess unobstructed porous channel, ca. 4 nm of wall thickness and high specific ratio area from 805 to 1065 m^2/g. These Y^{3+} and Eu^{3+} co-doped mesoporous silica show a widened emission band with the main peak located at 588 nm corresponding to the $^5D_0$–$^7F_1$ transitions and other four shoulder peaks, this broadening 4*f*–4*f* transition emission may mainly come from the nanometer amorphous wall of RE-SBA-15 with high specific surface area and a large amount of non-bridging oxygen around Eu^{3+} ions also plays important contribution, which enhances the relative intensity of magnetic-dipole $^5D_0$–$^7F_1$ transition of Eu^{3+} in RE-SBA-15. The work will pave a new method for preparation of detectable drug/gene carriers with high capacity.

Acknowledgments

This research was financially supported by the National Natural Science Fund of China (Grant nos. 20971021 and 20974018), Ph.D. Program Foundation of Ministry of Education of China (No. 20070255012), Shanghai Leading Academic Discipline Project (No. B603) and Open Project of the State Key Laboratory of Crystal Materials (KF0809), the Program of Introducing Talents of Discipline to Universities (No. 111-2-04).

References

[1] C.Y. Lai, B.G. Trewyn, D.M. Jeftinija, K. Jeftinija, S. Xu, S. Jeftinija, V.S.Y. Lin, J. Am. Chem. Soc. 125 (2003) 4451–4459.
[2] J. Kim, H.S. Kim, N. Lee, T. Kim, H. Kim, T. Yu, I.C. Song, W.K. Moon, T. Hyeon, Angew. Chem. Int. Ed. 47 (2008) 8438–8441.
[3] G. Kurlyandskaya, V. Levit, Mater. Sci. Eng. C—Biomimetic Supramol. Syst. 27 (2007) 495–503.
[4] S. Fuchs, H. Otto, S. Jehle, P. Henklein, A.D. Schluter, Chem. Commun. 14 (2005) 1830–1832.
[5] J. Hirvonen, Eur. J. Pharm. Sci. 34 (2008) S21.
[6] S. Angelos, M. Liong, E. Choi, J.I. Zink, Chem. Eng. J. 137 (2008) 4–13.
[7] M. Vallet-Regi, F. Balas, D. Arcos, Angew. Chem., Int. Ed. 46 (2007) 7548–7558.

[8] T. Heikkila, J. Salonen, J. Tuura, N. Kumar, T. Salmi, D.Y. Murzin, M.S. Hamdy, G. Mul, L. Laitinen, A.M. Kaukonen, J. Hirvonen, V.P. Lehto, Drug Delivery 15 (2007) 337–347.
[9] I.S. Carino, L. Pasqua, F. Testa, R. Aiello, F. Puoci, F. Iemma, N. Picci, Drug Delivery 14 (2007) 491–495.
[10] F.Y. Qu, G.S. Zhu, H.M. Lin, W.W. Zhang, J.Y. Sun, S.G. Li, S.L. Qiu, J. Solid State Chem. 179 (2006) 2027–2035.
[11] M. Vallet-Regi, A. Ramila, R.P. del Real, J. Perez-Pariente, Chem. Mater. 13 (2001) 308–311.
[12] V. Cauda, S. Fiorilli, B. Onida, E. Verne, C.V. Brovarone, D. Viterbo, G. Croce, M. Milanesio, E. Garrone, J. Mater. Sci:Mater. Med. 19 (2008) 3303–3310.
[13] L.B. Fagundes, T.G.F. Sousa, A. Sousa, V.V. Silva, E.M.B. Sousa, J. Non-Cryst. Solids 352 (2006) 3496–3501.
[14] S.W. Song, K. Hidajat, S. Kawi, Langmuir 21 (2005) 9568–9575.
[15] A.L. Doadrio, E.M.B. Sousa, J.C. Doadrio, J.P. Pariente, I. Izquierdo-Barba, M. Vallet-Regi, J. Controlled Release 97 (2004) 125–132.
[16] S.C.W. Richardson, K.L. Wallom, E.L. Ferguson, S.P.E. Deacon, M.W. Davies, A.J. Powell, R.C. Piper, R. Duncan, J. Controlled Release 127 (2008) 1–11.
[17] A. Agarwal, P.K. Tripathi, S. Tripathi, N.K. Jain, Curr. Drug Targets 9 (2008) 895–898.
[18] L.L. Li, D. Chen, Y.Q. Zhang, Z.T. Deng, X.L. Ren, X.W. Meng, F.Q. Tang, J. Ren, L. Zhang, Nanotechnology 18 (2007) 405102–405107.
[19] H.G. Zhu, M.J. McShane, J. Am. Chem. Soc. 127 (2005) 13448–13449.
[20] H.W. Song, H.Q. Yu, G.H. Pan, X. Bai, B. Dong, X.T. Zhang, S.K. Hark, Chem. Mater. 20 (2008) 4762–4767.
[21] C.K. Lin, D.Y. Kong, X.M. Liu, H. Wang, M. Yu, J. Lin, Inorg. Chem. 46 (2007) 2674–2681.
[22] L.L. Kong, B. Yan, Y. Li, J. Solid State Chem. 182 (2009) 1631–1637.
[23] S. Guang, C. Zhang, H. Xu, H. Wang, N. Lin. Chin, J. Inorg. Chem. 23 (2007) 999–1004.
[24] P.P. Yang, Z.W. Quan, C.X. Li, X.J. Kang, H.Z. Lian, J. Lin, Biomaterials 29 (2008) 4341–4347.
[25] P.P. Yang, S.S. Huang, D.Y. Kong, J. Lin, H.G. Fu, Inorg. Chem. 46 (2007) 3203–3211.
[26] M. Selvaraj, S. Kawi, Chem. Mater. 19 (2007) 509–519.
[27] A. Vinu, P. Srinivasu, M. Miyahara, K. Ariga hz, J. Phys. Chem. B 110 (2006) 801–806.
[28] M. Selvaraj, T.G. Lee, J. Phys. Chem. B 110 (2006) 21793–21802.
[29] A. Vinu, D.P. Sawant, K. Ariga, K.Z. Hossain, S.B. Halligudi, M. Hartmann, M. Nomura, Chem. Mater. 17 (2005) 5339–5345.
[30] S.Y. Chen, L.Y. Jang, S.F. Cheng, Chem. Mater. 16 (2004) 4174–4180.
[31] D.Y. Zhao, Q.S. Huo, J.L. Feng, B.F. Chmelka, G.D. Stucky, J. Am. Chem. Soc. 120 (1998) 6024–6036.
[32] P.D. Yang, D.Y. Zhao, D.I. Margolese, B.F. Chmelka, G.D. Stucky, Nature 396 (1998) 152–155.
[33] A.P. Jadhav, C.W. Kim, H.G. Cha, A.U. Pawar, N.A. Jadhav, U. Pal, Y.S. Kang, J. Phys. Chem. C 113 (2009) 13600–13604.
[34] C. Yang, P.P. Yang, W.X. Wang, S.L. Gai, J. Wang, M.L. Zhang, J. Lin, Solid State Sci. 11 (2009) 1923–1928.
[35] M. Yin, W. Zhang, S. Xia, J.C. Krupa, J. Lumin. 68 (1996) 335–339.
[36] M. Yin, C. Duan, W. Zhang, L. Lou, S. Xia, J.C. Krupa, J. Appl. Phys. 86 (1999) 3751–3757.
[37] W.S.B.J. Wang, J.R. Lincoln, lJ.E. Townsend, D.N. Payne, J. Non-Cryst. Solids 163 (1993) 261–267.